



Dynamics of carbon diffusion and segregation through nickel catalyst, investigated by in-situ XPS, during the growth of nitrogen-doped graphene

Y. Bleu, V. Barnier, F. Christien, F. Bourquard, A.-S. Loir, F. Garrelie, C. Donnet

► To cite this version:

Y. Bleu, V. Barnier, F. Christien, F. Bourquard, A.-S. Loir, et al.. Dynamics of carbon diffusion and segregation through nickel catalyst, investigated by in-situ XPS, during the growth of nitrogen-doped graphene. Carbon, 2019, 155, pp.410-420. 10.1016/j.carbon.2019.08.084 . hal-02280342

HAL Id: hal-02280342

<https://hal.science/hal-02280342>

Submitted on 20 Dec 2021

HAL is a multi-disciplinary open access archive for the deposit and dissemination of scientific research documents, whether they are published or not. The documents may come from teaching and research institutions in France or abroad, or from public or private research centers.

L'archive ouverte pluridisciplinaire **HAL**, est destinée au dépôt et à la diffusion de documents scientifiques de niveau recherche, publiés ou non, émanant des établissements d'enseignement et de recherche français ou étrangers, des laboratoires publics ou privés.



Distributed under a Creative Commons Attribution - NonCommercial 4.0 International License

Dynamics of carbon diffusion and segregation through nickel catalyst, investigated by in situ XPS, during growth of nitrogen doped graphene

Y. Bleu¹, V. Barnier², F. Christien², F. Bourquard¹, A.-S. Loir¹, F. Garrelie¹, C. Donnet^{1*}

(1) *Université de Lyon, Université Jean Monnet-Saint-Etienne, CNRS, Institut d'Optique Graduate School, Laboratoire Hubert Curien UMR 5516, F-42023, SAINT-ETIENNE, France*

(2) *Mines Saint-Etienne, Univ Lyon, CNRS, UMR 5307 LGF, Centre SMS, F - 42023 Saint-Etienne France*

Abstract

The mechanisms of diffusion and segregation of carbon from a solid carbon-based film, through a nickel film catalyst, was investigated using in situ, time- and depth-resolved X-ray photoelectron spectroscopy. The graphene precursor was a carbon nitride amorphous film obtained by pulse laser deposition. Changes in both surface and bulk sensitive carbon components versus annealing time was investigated at temperatures between 200 °C and 500 °C. A model of carbon diffusion/segregation through the nickel film was implemented, enabling the quantitative description of the graphene growth. Carbon diffusion through the nickel film was shown to occur at low temperatures (200-300 °C) and to induce the growth of graphene domains. The fine microstructure and high density of defects in the nickel catalyst film accelerated the transport of carbon, faster than conventional bulk diffusion. At 500 °C, bulk diffusion of carbon occurred, due to the recovering of the nickel grain microstructure. The diffusion/segregation model developed in this study can be used as a support to a better control of the growth and quality of the graphene. Our interpretations are discussed in relation to similar approaches related to graphene growth by chemical vapor deposition.

Keywords: Nitrogen-doped graphene, pulsed laser deposition, diffusion, segregation, in situ XPS

* Corresponding author. Email: Christophe.Donnet@univ-st-etienne.fr

1. Introduction

Among the processes used for graphene synthesis, some use a solid carbon precursor instead of a gas source as used in chemical vapor deposition (CVD). According to Weatherup et al.[1], catalytic graphitization of a solid carbon source is as versatile as CVD but is potentially simpler, cheaper and less hazardous. By monitoring the thickness of the carbon-based precursor, located on the underside of the metal catalyst or underneath, layer-by-layer graphene growth can be controlled by dissolution of carbon into the catalyst followed by precipitation, during a thermal process combining heating and cooling. Various methods have been explored to deposit and control the solid carbon source as a thin film precursor of graphene. Weatherup et al.[1] deposited an amorphous carbon-based film (10 nm) by filtered cathodic vacuum arc, followed by a nickel catalyst thin film, and focused on the role of an Al_2O_3 diffusion barrier sandwiched between the carbon under-layer and the nickel catalytic over-layer, to control the quality of a graphene monolayer obtained at temperatures as low as 600 °C. These authors observed that graphene growth mainly occurs during ramping up and annealing, by carbon dissolution and diffusion through the metal catalyst, indicating that the solid-state formation of graphene is not limited to carbon precipitation upon cooling. Magnetron sputtering was used by Xiong et al.[2,3] to explore the growth mechanism of graphene from a solid carbon source through a nickel metal catalyst layer. These authors used rapid thermal processing (RTP) to form mono-, bi- and tri-layer graphene, with precise control of the heating ramp, temperature and time of heating, depending on the thickness of both the carbon film precursor and the metal catalyst. They showed a solid-state reaction between metallic nickel and diffusing carbon forming a metastable nickel carbide compound at temperatures as low as 400°C, followed by its transformation into graphene layers associated with nickel sublimation at temperatures ranging from 800 to 1100 °C. Oldfield et al.[4] also used filtered cathodic vacuum arc (FCVA) to subsequently deposit a catalytic copper film and a carbon over-layer at a temperature of only 750 °C to induce graphene growth.

A significant number of publications report that pulse laser deposition (PLD) is of particular interest to control the composition of the carbon-based graphene precursor[5,6]. One of the main advantages of the PLD process is its versatility, which makes it possible to obtain specific compositions of carbon-based films, including incorporation of dopants or alloying elements with precise control of their concentrations, including nitrogen, boron, silicon, and metallic elements, as achieved by our group some years ago[7–12]. Compared to CVD

processes, such versatility is of particular interest when the aim is to obtain precise compositions of doped graphene for a variety of applications. As far as the incorporation of nitrogen in graphene is concerned, to our best of knowledge, only three papers report studies of the synthesis of nitrogen-doped graphene (NG) from a CN film obtained by PLD. Kumar et al.[13] produced p- and n-type graphene films using PLD in the presence of argon and nitrogen gas by ablating pyrolytic graphite. The electrical conductivity of the n-type NG film depended on the nitrogen pressure during growth, and a diode-like rectifying behavior was exhibited by p-n junction diodes produced using the graphene films. Ren et al.[14] controlled the concentration of nitrogen between 1.7 and 3.3 at% incorporated in graphene, as well as the nature of nitrogen hybridization by modulating the pressure of the nitrogen gas during graphite ablation at a substrate temperature of 780°C. Recently, using thermal heating of a CN film deposited by PLD, our group obtained nano-architected tri-layer nitrogen doped graphene with Bernal ABA stacking, with a nitrogen concentration up to 3at.% and dominant pyridinic hybridization[15].

Despite several reports on graphene synthesis using a solid carbon source and a metal catalyst, the atomic scale mechanism responsible for graphene synthesis requires more detailed investigation, particularly when a dopant is introduced in the carbon-based precursor. In the present work, we studied the growth mechanism of a nitrogen-doped graphene obtained by thermal heating of a typical CN film deposited by PLD. We used a powerful method consisting in coupling XPS acquisition during the vacuum thermal heating process at different temperatures and for different times.

The questions we aimed to answer are the following:

- What are the chemical forms of carbon and nitrogen, at the end of the high temperature annealing process and before cooling, responsible for the N-doped graphene growth (Part 3.1)?
- What are the kinetics of diffusion, through the nickel catalyst, of the different chemical forms of carbon during thermal annealing, at the range of temperatures and times investigated (Part 3.2)?
- Can a diffusion model highlight the diffusion pathways of carbon, as a function of the annealing conditions (Part 3.3)?

We compare our results and interpretations related to N-doped graphene growth from a solid nitrogen-containing carbon source with the mechanisms of pure graphene growth on a metal

catalyst, investigated in particular by Weatherup et al., based on a CVD process[16–18], as well from a solid carbon source beneath the nickel catalyst[1].

2. Experimental

Synthesis of a-C:N films by pulsed laser deposition (PLD). SiO₂ substrates ultrasonically cleaned first in acetone then in ethanol and deionized water baths were introduced in a vacuum chamber pumped at a base pressure of 10⁻⁵ Pa. Amorphous carbon films were deposited by femtosecond pulsed laser deposition at room temperature with a nitrogen dose of about 4%, as controlled by XPS. A femtosecond oscillator at the 800 nm wavelength, with a pulse duration of 60 fs and a repetition rate of 1 kHz, delivered a laser beam focused at an angle of 45° onto a high purity graphite target (99.9995% purity). The energy density (fluence) of the laser beam was kept constant at 5 J/cm², with a nitrogen gas pressure of 10 Pa during the ablation process. The ablation time was adjusted to keep an a-C:N film thickness of 10 nm. The SiO₂ substrates were mounted on a sample holder placed at a distance of 40 mm from the graphite target.

Synthesis of Ni catalytic films onto the a-C:N film. Following deposition of the carbon film, a 150 nm thick nickel film was deposited by thermal evaporation on top of the a-C:N film. High purity (99.99%) Ni was melted thermally in a tungsten nacelle and evaporated at a base pressure of 10⁻⁴ Pa towards the substrate. The deposition rate was set at 1.5 nm/minute to minimize residual stress in the growing film, thereby limiting film delamination.

In situ thermal annealing coupled with X-ray photoelectron spectroscopy (XPS) analysis. The Ni/a-C:N/ SiO₂ samples were heated at 200, 300 and 500 °C with a heating ramp rate of 1 °C/s, in an ultrahigh vacuum pressure of 10⁻⁷ Pa, inside the chamber of the XPS apparatus, as summarized in **Table 1**. The samples being analyzed were subjected to thermal treatment using a resistive heater incorporated in the sample holder in order to obtain time-resolved recordings of C1s and Ni2p_{3/2} core levels. The temperature was controlled using a combination of a thermocouple in contact with the surface of the sample, and a pyrometer. For time resolved analyses, fast acquisition of C1s and Ni2p_{3/2} was performed in snapshot mode using the 128 channels of the energy dispersive 2d detector axe. Before in-situ annealing, a slight Ar⁺ sputtering was performed followed by a survey spectrum (0-1400 eV) in order to check that only Ni was detected at the surface of the sample. For each thermal treatment, no other elements were detected at this step.

XPS analyses were performed with a Thermo VG Thetaprobe spectrometer (Thermo Fisher Scientific). XPS analysis was carried out with a focused monochromatic AlK α source ($h\nu = 1486.68$ eV, 400 μm spot size) and photoelectrons were collected using a concentric hemispherical analyzer operating in the constant ΔE mode and a 2D channel plate detector. The energy scale was calibrated with sputter-cleaned pure reference samples of Au, Ag and Cu such that Au4f $_{7/2}$, Ag3d $_{5/2}$, and Cu3p $_{3/2}$ were positioned at binding energies of respectively 83.98, 386.26 and 932.67 eV.

Angle-resolved XPS measurements were performed at the end of each treatment just before cooling, with an analyzer pass energy of 50 eV. This pass energy gives a width of the Ag3d $_{5/2}$ peak measured on a sputter clean pure Ag sample of 0.55 eV. It is worth noting that these measurements were acquired thanks to the ability of spectrometer to simultaneously collect several photo-electron emission angles in acceptance range of 60° without tilting the sample. Components of the C1s peak were adjusted using line shapes consisting of a convolution product of a Gaussian function (75%) and Lorentzian function (25%) for C_{dis} and C_{carbides} and asymmetric lines shapes for C_{Gr} and C_B components for which parameters (tail percentage, height, and exponent) were adjusted on analyzed pure HOPG reference sample.

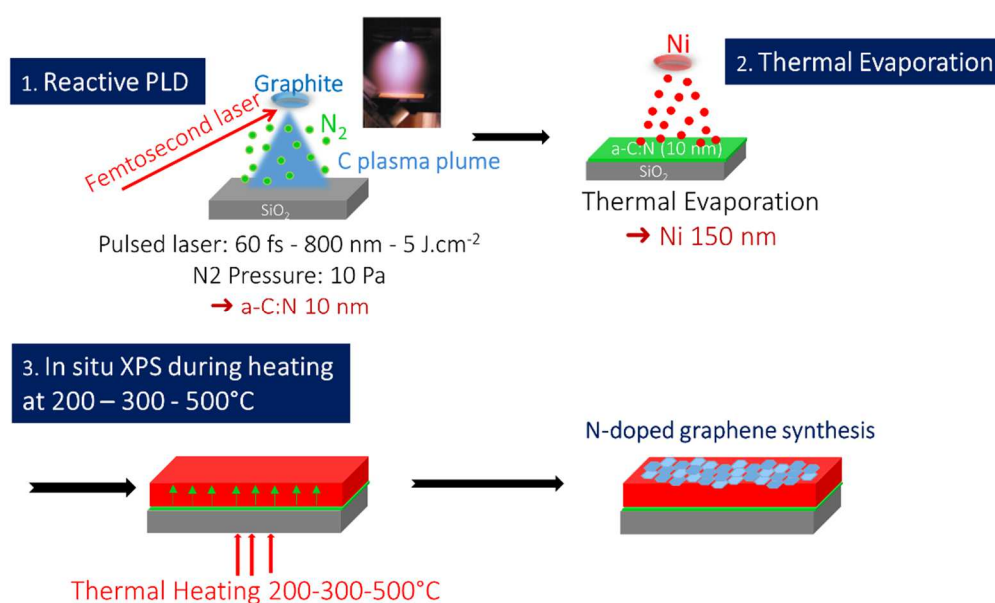


Figure 1. Synthesis process of N-doped graphene films, by thermal heating of a Ni/a-C:N/SiO₂ with in situ XPS analysis.

Ex situ analysis. Raman spectroscopy was performed using an Aramis Jobin Yvon spectrometer at 442 nm, with a spectral resolution of 2 cm^{-1} as recorded on a CCD camera, and a lateral resolution of $\sim 1\text{ }\mu\text{m}$. The laser beam is focused with a 100x objective, consistent with a laser spot diameter of less than $1\text{ }\mu\text{m}$ for both wavelengths. The laser power was kept below 3 mW to avoid damaging the film surface. A custom-made algorithm relying on the SciPy python library was used to extract the intensity, width, and position of the Raman peaks. Most peaks are fitted using Lorentzian functions, except for the G peak which is fitted with a Breit-Wigner-Fano function accounting for its asymmetry compared to a classical Lorentzian profile. When computing later intensities ratios, we will be referring, as is usually the case in the literature, to the peak height (intensity maximum) as opposed to its area. Complementary ex situ characterizations were performed by field-emission gun scanning electron microscopy (FEI Novanano SEM 200) operating at 15 kV. **Electron Back Scattered Diffraction (EBSD) was carried out in an other scanning electron microscope (Zeiss Supra55 FEG-SEM) equipped with an EBSD system from HKL-Oxford Instruments.**

Annealing temperature, T	Time of annealing at temperature T	In situ analysis during annealing	Ex situ analysis
200 °C	23 460 s	XPS	None
300 °C	22 760 s	XPS	Raman, SEM, EBSD
500 °C	4 980 s	XPS	Raman, SEM, EBSD

Table 1. Experimental conditions for thermal heating of Ni/a-C:N/SiO₂ films, with in situ XPS during heating and ex situ complementary experiments. For each temperature, a ramp of 1°C/s was scheduled to reach the annealing temperature indicated in column 1.

3. Results and discussion

3.1. Chemistry of carbon and nitrogen after diffusing across the nickel layer

The graphene films obtained by thermal heating at 300 °C and 500 °C were investigated by Raman spectroscopy after the annealing process (performed inside the XPS spectrometer), in order to check the typical signatures of graphene. The interpretation of the D ($1,350\text{ cm}^{-1}$), G (1580 cm^{-1}) and 2D (2700 cm^{-1}) bands is based on the literature[19,20]. **Figure 2a** shows the spectra and **Table 2** lists the corresponding D, 2D and G band positions and ratios, as well as the FWHM of the 2D band and the correlation length L_a , deduced from the Tuinstra-Koenig relation[21]. At 300 °C (after 6 h 24 min of thermal annealing), a wide low 2D band was detected, consistent with the presence of a high defective graphene-like structure, far from

typical graphene whose signature is a high narrow 2D band, as well as a low D band. This observation may be consistent with some carbon diffusing from the carbon underlayer through the nickel catalyst (as it will be shown later by in situ XPS during the heating process) and stabilized in the sp^2 hybridization on the top surface. At 500 °C (after 1 h 31 min of thermal annealing), the 2D band was consistent with the formation of few-layer graphene, considering a I_{2D}/I_G ratio of 0.36, a FWHM(2D) of 96 cm^{-1} and a I_D/I_G ratio of 0.12 consistent with a correlation length of 76 nm. **Figure 2b** shows the Raman mappings of the I_{2D}/I_G and I_D/I_G ratios for the graphene film obtained at 500°C. The region related to the spectrum depicted in **Figure 2a** is localized by a white mark in the Raman mapping. Average values of the ratios I_{2D}/I_G and I_D/I_G are 0.30 and 0.23 respectively. The I_{2D}/I_G ratio is consistent with a stacking of 3-5 layers (as confirmed further by XPS), rather homogeneous considering a standard deviation of 0.09 deduced from the 100 Raman spectra of the mapping. However, the distribution of defects over the probed area is more heterogeneous, considering a standard deviation of 0.17 for the I_D/I_G ratio.

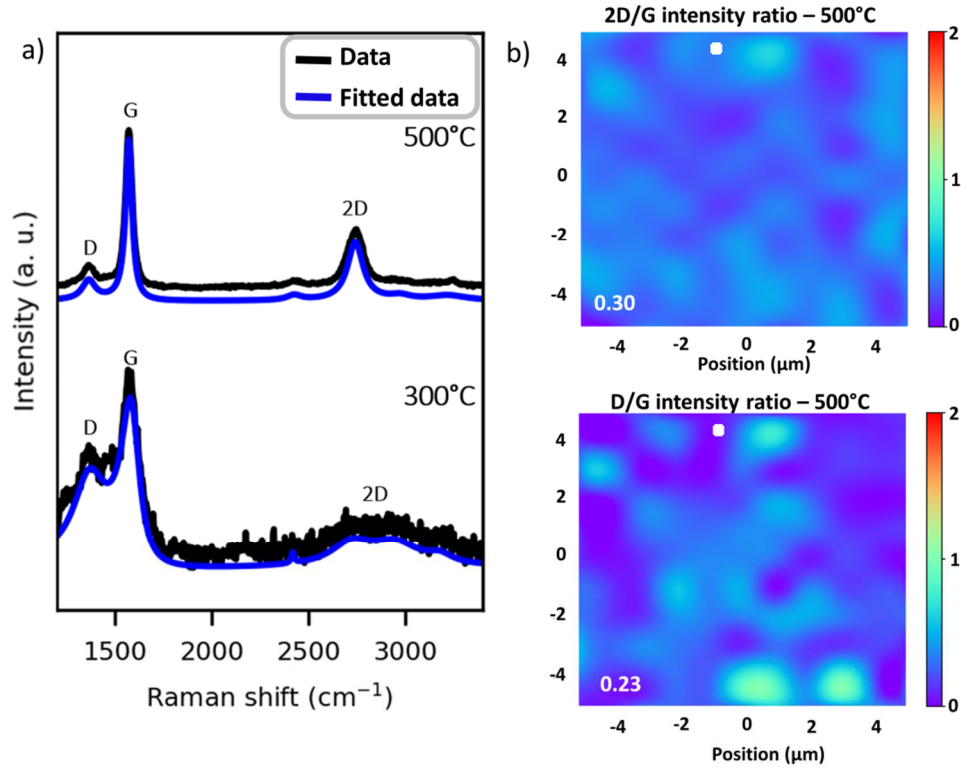


Figure 2. a) Raman spectra of the N-doped graphene films after heat treatments at 300 °C (22 760 s) and 500 °C (4980 s) in ultrahigh vacuum; b) Raman mappings (10 x 10 μm^2) of the 2D/G and D/G intensity ratios related to the N-doped graphene film synthesized at 500°C. The white mark corresponds to the location of the spectrum depicted in (a). The values 0.30 and 0.23 correspond to the mean values of the 2D/G and D/G intensity ratios respectively, over each mapped area.

Annealing temperature	300 °C	500 °C
D position	1370 cm^{-1}	1367 cm^{-1}
G position	1587 cm^{-1}	1574 cm^{-1}
2D position	2714 cm^{-1}	2742 cm^{-1}
I_{2D}/I_G	0.17	0.36
I_D/I_G	0.51	0.12
FWHM(2D)	230 cm^{-1}	96 cm^{-1}
Correlation length L_a	18 nm	76 nm

Table 2. Raman characteristics deduced from the spectra depicted in Figure 2.

The chemistry of carbon was investigated assigning four components in the C1s spectrum based on previous interpretations related to graphene films obtained by using metallic

catalyst[1,15] and the work of Weatherup and al.[17] who considered the graphene-catalyst interaction on the basis of the binding energy shift of the graphitic (C_{sp^2}) component. Taking into account this interaction, we consequently also considered two components for graphene: a component C_{Gr} at 284.4 +/-0.1 eV for weakly interacting graphene layers and a component C_B at 284.8 +/- 0.1 eV for graphene that strongly interacts with Ni catalyst. The function and parameters (binding energy, full width at half maximum, peak asymmetry) for the C_{Gr} and C_B components were determined using C1s spectrum measured on pure HOPG reference sample. The two other contributions considered in the C1s peak were a component C_{dis} at 283.8 +/-0.1 eV corresponding to carbon in solid solution Ni(C) interstitially dissolved in the metal catalyst, and a component $C_{carbide}$ at 282.9 +/-0.1 eV associated with the precipitation of nickel carbides.

Figure 3a shows typical adjustment using the four previously described components of **C1s** spectra recorded in XPS angle resolved mode for two photoelectron take-off angles at the end of thermal annealing at 500 °C (i.e. before cooling). Similar analyses were carried out for annealing treatments at 200 °C and 300 °C. Comparison of the **C1s** peak fitting for a photoelectron take-off angle of 35° with the one at a take-off angle of 65° for which the depth of analysis is reduced, indicates a difference in the proportions of the component and rules out inhomogeneous distribution. **Figure 3b** shows the logarithm of the ratio of 35° “bulk sensitive” and 65° “surface sensitive” emission angle intensities for each **C1s** components. Considering that the signal from a species arises from a layer buried beneath a layer of depth d , this value can also be expressed as follows:

$$-\ln\left(\frac{I_{35^\circ}}{I_{65^\circ}}\right) = d \left[\left(1/\lambda \cos(35^\circ)\right) - \left(1/\lambda \cos(65^\circ)\right) \right] \quad (\text{Eq.1})$$

Assuming the same electron inelastic mean free path λ for the different components, the logarithm of the intensity ratio gives a direct measurement of the relative value of d . **Figure 3b** presents the relative depth plot of the four **C1s** components and shows that C_{Gr} and C_B components are surface sensitive, while $C_{carbide}$ and C_{dis} components are bulk sensitive (the $C_{carbide}$ component being more bulk sensitive than the C_{dis} component). Similar results were also found for angle-resolved measurements after annealing treatment at 200 °C and 300 °C. Based on these observations, a schematic distribution of the different carbon species is proposed in **Figure 3c**. The C_{Gr} and C_B surface sensitive components are associated with the segregation of carbon and the growth of graphene layers at the surface of the sample. The

weakly interacting graphene layers tied to the C_{Gr} component is considered as additional graphene layers or rotated graphene, while C_B is considered as strongly interacting epitaxial graphene[17,22]. This difference in interaction is confirmed on the relative depth plot of the **Figure 3b**, with a component C_{Gr} slightly more sensitive to the surface than C_B . On the other hand, the $C_{carbide}$ component is clearly bulk sensitive and may arise from the formation of nickel carbides homogeneously distributed on the XPS depth of analysis. It is worth noting that at the binding energy of the $C_{carbide}$ component, i.e. close to 283 eV, these carbides are generally assigned to metastable Ni_3C [23] from which graphene growth mechanism can be involved in solid state[3,24].

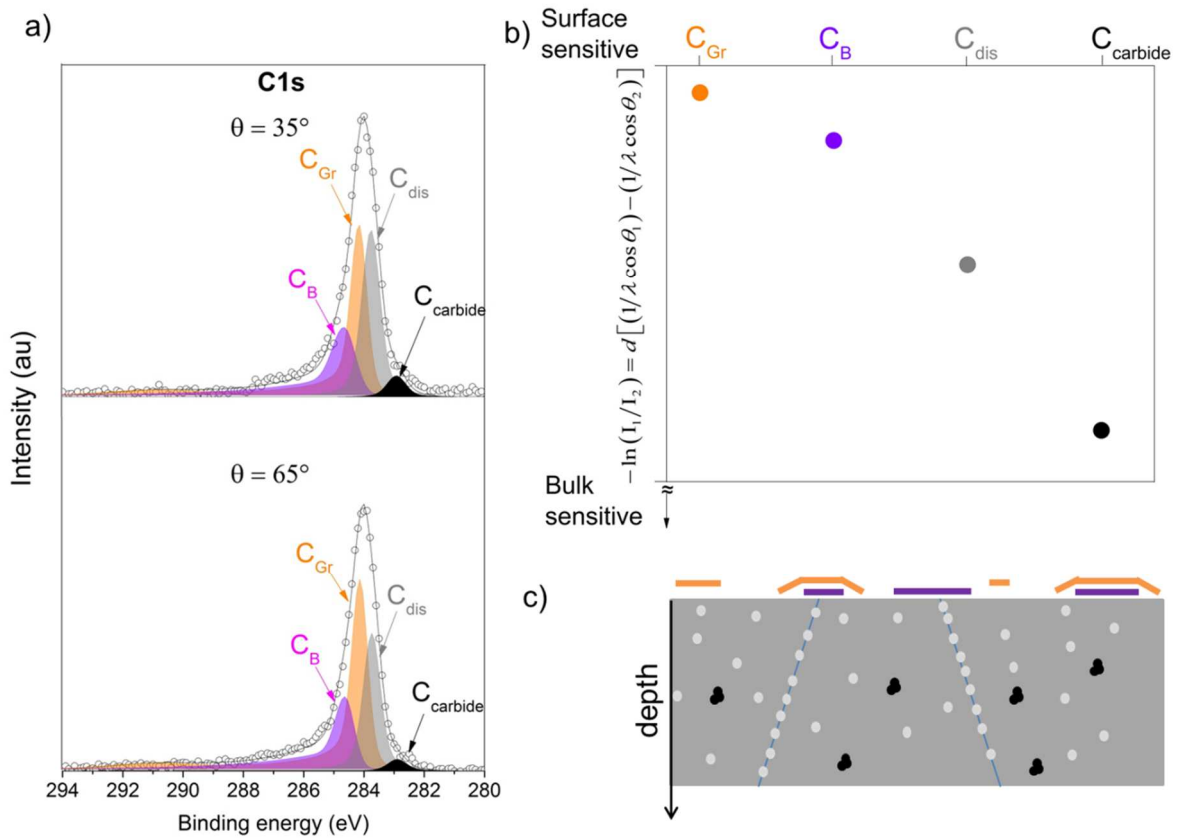


Figure 3: Angle-resolved XPS analyses of C1s at the end of annealing treatment at 500 °C before cooling: a) adjustments of C1 peaks at two photoelectron escape angles using the components described in [17], b) *relative depth plot based on the logarithm of the ratio of intensities at $\theta=35^\circ$ and $\theta=65^\circ$, and indicating the relative sensitivity to the surface of each component used to adjust C1s*, c) *Schematic in-depth distribution based on the relative depth plot results of the carbon species: graphene weakly interacting with Ni “component C_{Gr} ” represented by orange lines, graphene strongly interacting with Ni “component C_B ” represented by purple lines, carbide “component $C_{carbide}$ ” represented by black spheres, and carbon dissolved “component C_{dis} ” represented by black spheres.*

Figure 4 shows a typical adjustment, using four components, of N1s spectra at the end of thermal annealing at 500 °C (i.e. before cooling). The N/(N+C) ratio deduced from XPS

analysis is 4 at.%. The four components observed on the N1s spectrum are interpreted based on[25] and our previous work[15]. Pyridinic, pyrrolic, and quaternary (or graphitic) nitrogen configuration in the N-doped graphene films were detected at 398.2, 400.1, 401.5 eV respectively, with a predominance of the pyrrolic configuration. An additional pyridinic oxide configuration was detected at a higher binding energy of 403.9 eV. The C_B and C_{Gr} components certainly include the carbon-nitrogen bonds, but the low nitrogen concentration of 4 at.% did not enable identification of their contribution. It is also worth to mention that nickel nitrides which were evidenced by a N1s peak at a binding at 395.8 eV[26] were not detected which involves that no or few amount of nitrides (< 0.1 %at) was formed during thermal annealing.

The analysis of the chemistry of carbon and nitrogen diffusing from the a-C:N film across the nickel layer revealed that the model of carbon diffusion and interaction with the Ni catalyst, the presence of carbides and subsurface carbon species described in the case of pure graphene growth obtained from chemical vapor deposition[17] is in accordance with what we observed in the case of growth mode using a solid carbon based source. Moreover, the presence of nitrogen in the source made it possible to produce 4% nitrogen doped graphene. N1s signal shows the chemical compositions at different energy levels: pyridinic N bond at 398.2 eV, pyrrolic N bond at 400.1 eV, quaternary N at 401.5 eV and pyridinic oxide N at 403.9 eV in agreement with References[25,27–29]. Our nitrogen content is comparable with what was found using hydrothermal method[29] and thermal exfoliation of graphite oxide for graphene doping with nitrogen[27].

In order to evaluate the kinetics of graphene growth and also to consider the changes in and interactions between the carbon species highlighted above, time-resolved XPS analyses were performed.

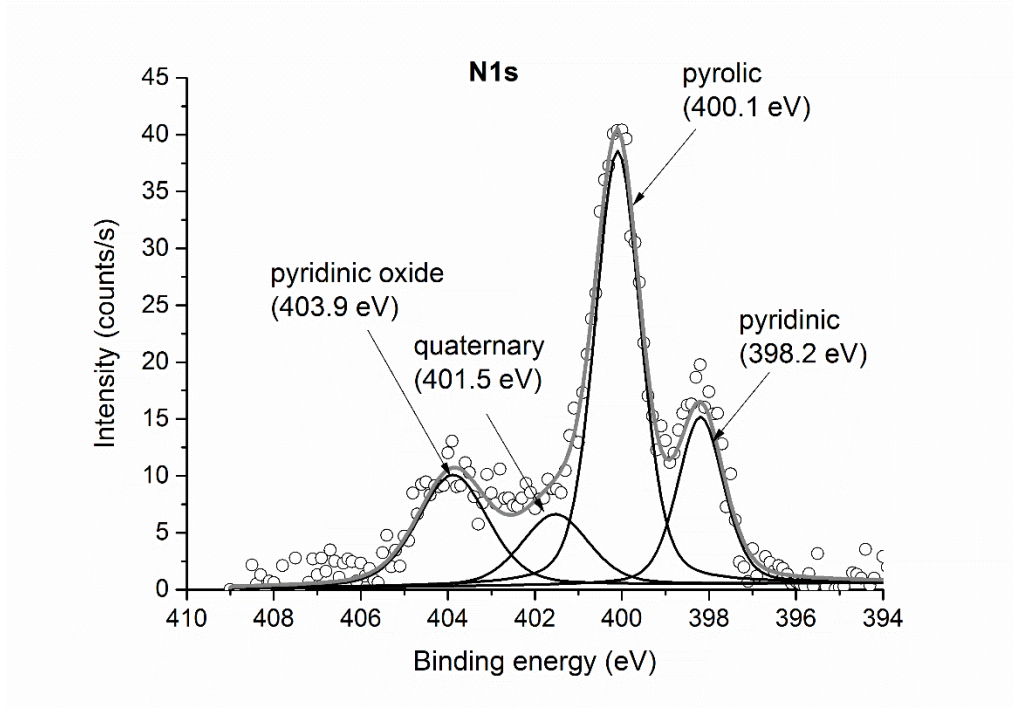


Figure 4: N1s peak recorded at the end of annealing treatment at 500 °C before cooling.

3.2. Kinetics of carbon diffusion across the nickel film

Fast acquisition of C1s and Ni2p_{3/2} photoelectron peaks, using the snapshot spectrometer detector mode, were performed during in situ thermal annealing. Unfortunately, the low concentration of nitrogen in the graphene film (4 at.%) could not record the N1s photoelectron peaks using the snapshot mode due to a too low intensity during the thermal annealing process. In the case of the C1s peak, the same function parameters defined previously for analyses of the angle resolved spectrum were used to fit the components C_{Gr}, C_B, C_{dis} and C_{carbide}. Considering the distribution of the different carbon species presented in **Figure 3**, the C_{Gr} and C_B components intensities were converted into monolayers using the following equations (In (Eq.2), C_{comp} represents either C_{Gr}, either C_B):

$$C_{comp}(\text{monolayer}) = \frac{I_{C1s}^{C_{comp}}}{I_{C1s}^{HOPG} \times \left(1 - \exp\left(\frac{-d}{\lambda_{C1s}^{layer} \cos \theta} \right) \right)} \quad (\text{Eq.2})$$

where I_{C1s}^{HOPG} is the intensity of the C1s peak measure on a pure HOPG reference sample, $d=0.335$ nm is the thickness of a graphene monolayer, λ_{C1s}^{layer} the inelastic mean free path of a photoelectron coming from the core level C1s and travelling through a graphene layer for

which we chose a value of 1.2 nm based on the work of Tyagi et al.[30] and θ the photoelectron escape angle with respect to the normal of the sample surface.

As the C_{dis} and $C_{carbide}$ components were assumed to be only distributed in the catalyst substrate, the intensities were converted into atomic percentage using the intensity of $Ni2p_{3/2}$ and the following expressions equations (In Eq.3, C_{comp} represents either C_{dis} , either $C_{carbide}$):

$$C_{comp} (\%at) = \frac{I_{C1s}^{C_{comp}} / F_{C1s}}{I_{C1s}^{C_{comp}} / F_{C1s} + I_{Ni2p_{3/2}} / F_{Ni2p_{3/2}}} \quad (Eq.3)$$

$$F_A = \lambda_A^{sub} \times \sigma_A \times T_A \times \left[\tau \times \left(\exp\left(\frac{-d}{\lambda_A^{layer} \cos \theta}\right) - 1 \right) + 1 \right] \quad (Eq.4)$$

where $\lambda_A^{(sub,layer)}$ is the inelastic mean free path of a photoelectron coming from the core level A (A being either C1s, either $Ni2p_{3/2}$) in the substrate “sub” or in the carbon segregated surface film “layer”, σ_A is the Scofield ionization cross section of core level A, T_A the transmission function at the kinetic energy of the photoelectron coming from the core level A, d is the thickness of the carbon segregated layer and θ is the photoelectron escape angle with respect to the normal of the sample surface. The values of the inelastic mean free path in the segregated carbon film were chosen based on the work of Tyagi and al.[30], and those in the substrate were estimated with the TPP2M method[31]. The results are presented in **Figure 5** which represents the fraction of monolayer or atomic percentage of the four **C1s** components as a function of the square root of the time since we can consider that the kinetics of the four components are driven by the diffusion of carbon across the Ni layer.

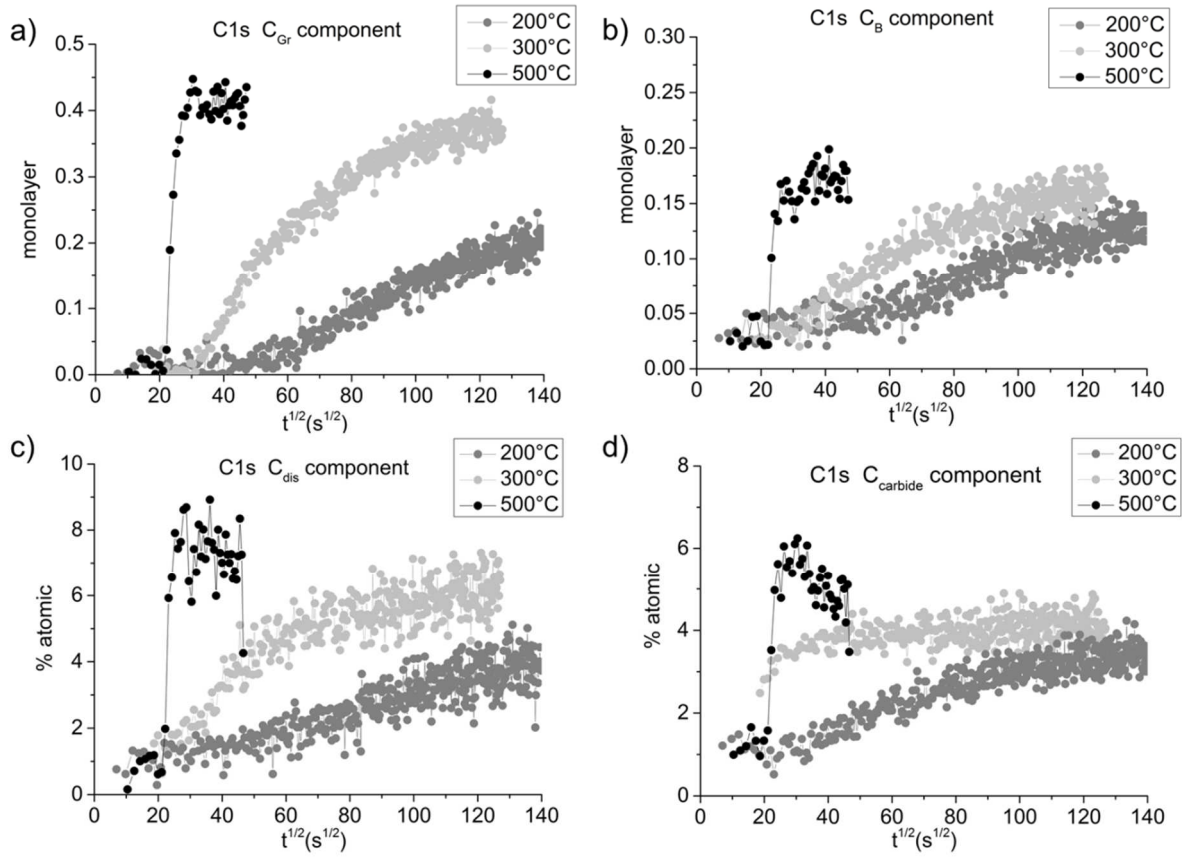


Figure 5: Changes in function of the square root of the time of surface sensitive components C_{Gr} and C_B of C1s core level expressed as a fraction of the monolayer using Eq.2 and bulk sensitive components $C_{carbide}$ and C_{dis} expressed in atomic percent units using Eq.3.

Figures 5a-b show changes in the fraction of monolayer of graphene weakly interacting with the nickel catalyst (C_{Gr}) during annealing, and graphene which interacts strongly with the nickel catalyst (C_B). These changes indicate the presence of both types of carbon components even at a temperature as low as 200 °C. It is worth noting that unambiguous graphene Raman signature was only detected at 500 °C (**Figure 2**). This can be explained by the small spatial extent of sp^2 regions at low temperature and the fact that XPS is more sensitive to local bonding than Raman while the latter is sensitive to the organization, extent and crystallite size of graphene domains[32]. The changes in C_{Gr} and C_B also suggest that at low temperatures, the diffusion is abnormally fast since the C_B component was detected at the surface after less than one hour ($< t^{1/2} = 60 \text{ s}^{1/2}$) at $T=200 \text{ °C}$. This point is discussed in the following section. We also note that the fraction of monolayer for each component never exceeds a complete monolayer even when both contributions are summed, which can be partly explained by the

distribution of surface crystallographic orientations some of which are more favorable for the growth of graphene. In particular, with weak lattice mismatch of 1.3%, Ni(111) is ideal for growing epitaxial graphene[33]. Electron backscattering diffraction orientation map along sample's Z direction of sample annealed at 300°C and 500°C are presented in Figures 6d) and e) indicating a similar average grain size of 200 nm and a (111) texture for both thermal treatments. Finally, at 500 °C, the presence of a plateau highlights a self-limited reaction that can be described by the diffusion/segregation model. The changes in C_{carbide} , shown in **Figure 5c**, show the progressive formation of carbides at 200 °C and 300 °C that tends toward a value of 4%. At 500 °C, C_{carbide} first exceeds this value and then starts to decrease due to decomposition of the metastable carbide. Note that the C_{dis} component appears to be stable when the carbides start to decompose, suggesting that the released carbon does not remain in solid solution but is probably used for graphene growth. Compared to the C_{Gr} component, which clearly shows no change at $t^{1/2} = 30 \text{ s}^{1/2}$, C_{B} appears to increase slightly, suggesting that the released carbon is used for growing graphene strongly interacting with Ni. **Figure 5d** shows changes in the C_{dis} component that exhibits atomic percent values in the order of few percent at the three thermal annealing temperatures (7% at $T=500 \text{ °C}$) which represents a large amount of carbon if we consider that this component reflects the presence of dissolved carbon. In particular, the expected equilibrium carbon in solid solution for Ni at room temperature is <0.01 at% and in the order of 0.1 at% at 500 °C[34,35]. As we already mentioned, one assumption is to consider that carbon is segregated at Ni grain boundaries. Analyses of Ni grain size using scanning electron microscopy and electron backscattering diffraction **Figure 6 b-e)** showed an average grain size of 200 nm at the end of 300°C and 500°C thermal treatments. Considering the thickness of Ni film with surface equiaxed grains is 150 nm, if the carbon fills all the grain boundaries, this gives an average value of 0.1 atomic percent. This assumption consequently fails to explain the large values associated with the C_{dis} component.

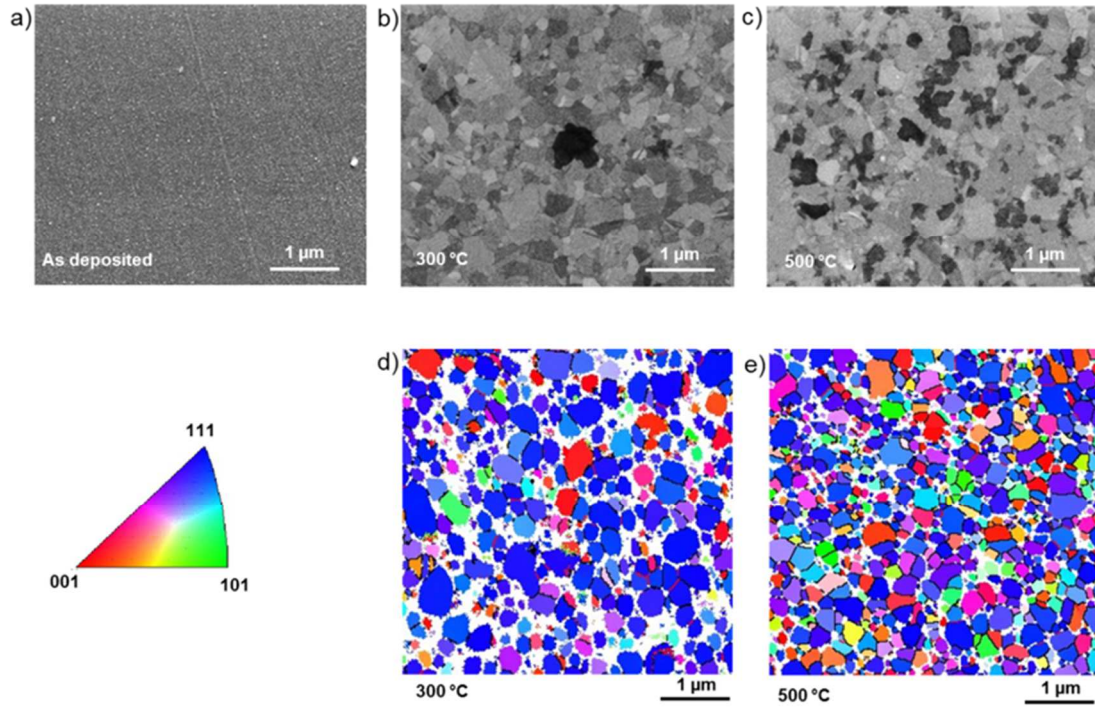


Figure 6: SEM pictures of: a) the as-deposited Ni/a-C:N/SiO₂ before annealing b) after annealing at 300 °C and c) after annealing at 500 °C performed in ultrahigh vacuum in the XPS chamber. Electron backscattering diffraction orientation map along sample's Z direction of d) sample annealed at 300°C and e) 500°C.

Another possible explanation for the high concentration of dissolved carbon is the type of carbon source used in this study, which was amorphous carbon. The measurements of carbon solubility in nickel available in the literature are based on systems in which the source of carbon is graphite[34,35], not amorphous carbon. It has been demonstrated that the chemical potential of carbon is significantly higher in amorphous carbon than in graphite[35], which means that the amount of carbon expected to dissolve into nickel is higher when amorphous carbon is used, rather than graphite. This could explain why the concentration of carbon dissolved in nickel is so large in our study.

The amount of dissolved carbon in the nickel catalyst is of prime importance because of its interaction with graphene. In particular, using in-situ XPS measurements and grand canonical Monte Carlo simulation, Weatherup et al.[17] showed that, depending on the amount, the dissolved carbon can:

- weaken the interaction between an epitaxial graphene layer and the catalyst leading to the growth of an additional second layer at the interface between the catalyst and the existing graphene layer,
- affect the interaction and thus the epitaxy of the graphene as it forms.

Since the work of Weatherup et al.[1] was based on a chemical vapor deposition method, we wanted to see if this behavior applies equally to graphene synthesis via a solid carbon source. **Figure 7** shows the influence of the amount of carbon in solid solution on the growth of graphene layers. The figure plots the C_{Gr}/C_B ratio of the fraction of the monolayer of weakly interacting graphene with the nickel catalyst, to the one strongly interacting graphene, as a function of the atomic percentage of carbon in solid solution C_{dis} associated with this ratio at each time of the kinetics, at the three annealing temperatures. The plot shows three domains:

- a domain for an amount of dissolved carbon < 2 at% where the ratio is weak, and consequently most of the growing graphene is in the form of islands of monolayer epitaxial graphene, with the main contribution coming from C_B (inset (a) in **Figure 7**).
- a domain for an amount of dissolved carbon between 2 and 4 at% where the ratio is in the range of 1.3 to 1.5. If we consider a second layer growing between the catalyst and the original islands of graphene monolayers, the ratio of C_{Gr} to C_B should be equal to $\exp(d/\lambda/\cos\theta) = 1.54$. This suggests that in this domain, additional dissolved carbon promotes the progressive growth of bilayer islands (insets (b) and (c) in **Figure 7**).
- a domain for amounts of dissolved carbon > 4 at% where the C_{Gr} to C_B ratio is close to 2.5. Such high concentrations of dissolved carbon in Ni additionally favor the formation of weakly interacting graphene (C_{Gr}) (inset (d) in **Figure 7**), as observed by Weatherup et al.[17] by using CVD synthesis (and called “rotated graphene” by these authors).

In summary, the analysis of kinetics of carbon diffusion highlights the following points. The diffusion of carbon across the Ni catalyst layer is very fast, giving rise to the formation of small graphene islands on the surface of the nickel grains, even at low temperatures. The diffusion of carbon triggers the formation of metastable nickel carbides that quickly reach equilibrium at low temperatures but start to decompose at 500 °C, implying that nickel carbides are not the major source involved in the formation of graphene at temperature $< 500^\circ\text{C}$. The behavior of the C_{dis} component reveals that the Ni subsurface is oversaturated with carbon with amounts than can reach 7at% at 500 °C. Even though it is impossible to

unambiguously define the nature of these subsurface carbon atoms (interstitially dissolved or Ni_2C), their presence appears to influence the graphene growth mechanism as already reported in the chemical vapor deposition method[17]. In particular, three domains of subsurface carbon content were identified at a low temperature ($T < 500^\circ\text{C}$). **Because the presence of graphene and subsurface carbon atoms originate from carbon of the a-C:N source diffusing across the Ni layer, a diffusion/segregation model was developed to fit the XPS measurements.**

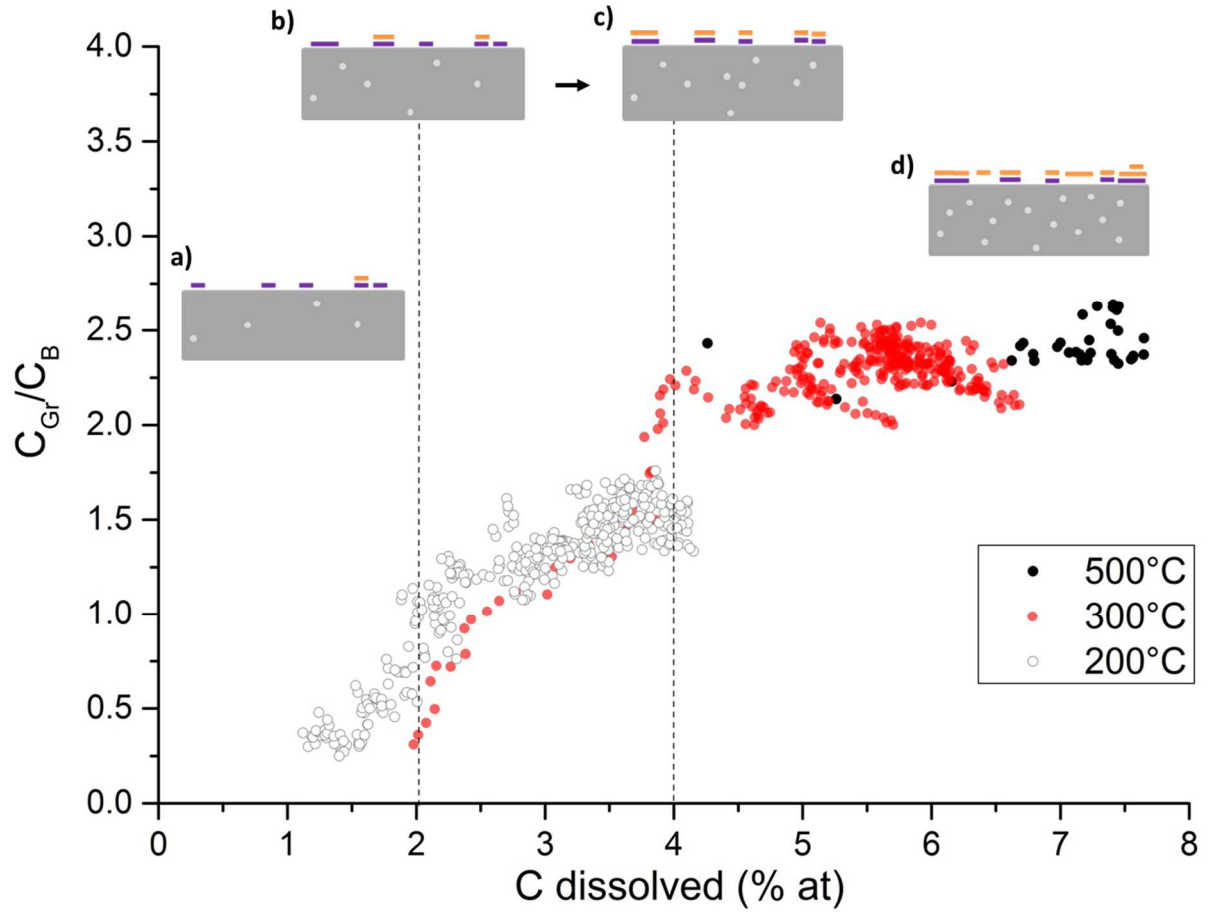


Figure 7: ratio of the fraction of the C_{Gr} to the C_B component as a function of dissolved carbon based on the kinetics data at 200, 300 and 500 $^\circ\text{C}$ (Figures 5 a, b and d). The sketches a, b, c, and d indicate the effect of C dissolved on the growth of strongly catalyst interacting graphene layer (purple) and weakly catalyst interacting graphene layer (orange) for the ranges delimited by dotted lines: a domain for an amount of dissolved carbon < 2 at% where most of the growing graphene is in the form of islands of monolayer epitaxial graphene (sketch a), a domain between 2 and 4 at% where additional dissolved carbon promotes the progressive growth of bilayer islands (sketch b -> sketch c) and a domain for amounts of dissolved carbon > 4 at% where the formation of weakly interacting graphene is promoted (sketch d).

3.3. Modeling the diffusion and segregation of carbon through the nickel film

3.3.1. Background

The model is illustrated in **Figure 8**. Amorphous carbon located below the nickel film is considered as an infinite source of carbon. The concentration of dissolved carbon C_i on the underside of the nickel film, i.e. close to the a-C/Ni interface, is fixed (Dirichlet boundary condition). This term is adjusted for each temperature but is considered constant over time during annealing at a given temperature. Carbon diffusion across the nickel film is calculated using the usual 2nd Fick's law (Eq.5):

$$\frac{\partial C}{\partial t} = D \frac{\partial^2 C}{\partial x^2} \quad (\text{Eq.5})$$

Where C is the carbon concentration (m^{-3}) at depth x and D is the carbon diffusion coefficient in nickel ($\text{m}^2 \text{s}^{-1}$). The formation of a carbon-rich film on the surface of nickel is treated here as a surface segregation phenomenon. The two types of carbon located at the surface (C_{Gr} and C_B) are considered here as "surface segregated" carbon. The model used here to describe carbon surface segregation is based on the Darken-du Plessis approach for interface segregation, which is described in details in several refs[36,37]. This approach has been successfully tested in various complex surface segregation conditions[38–41]. The flux J of carbon ($\text{m}^{-2} \text{s}^{-1}$) from nickel to the segregated layer is given by (Eq.6):

$$J = \frac{DC_1}{RT} \frac{\partial \mu}{\partial x} \quad (\text{Eq.6})$$

where T is the temperature (K), R is the gas constant ($R = 8.314 \text{ J mol}^{-1} \text{ K}^{-1}$), C_1 is the carbon concentration (m^{-3}) in nickel in contact with the segregated carbon (see **Figure 8**) and $\partial \mu / \partial x$ is the gradient of carbon chemical potential at the interface between the nickel and the segregated layer. ∂x depends on the mesh size chosen in the calculation. $\partial \mu$ is given by (Eq.7):

$$\partial \mu = -\Delta G - RT \ln \frac{\theta}{X_1(1-\theta)}, \quad \text{with } X_1 = C_1 / C_{Ni} \text{ and } \theta = C_s / C_{Max} \quad (\text{Eq.7})$$

where ΔG is the surface segregation free energy of carbon, X_1 and C_1 are respectively the molar fraction and the concentration (m^{-3}) of carbon in nickel in contact with the segregated carbon, C_{Ni} is the number of nickel atoms per unit volume of nickel (m^{-3}), C_s is the carbon concentration in the segregated layer (m^{-2}), C_{Max} is the maximum carbon concentration possible in the segregated layer. The structure of the segregated layer is treated here as a graphene layer so that C_{Max} is the number of carbon atoms per unit surface in a full graphene layer ($3.82 \cdot 10^{19} \text{ m}^{-2}$). θ is the coverage ratio. Eq.7 is derived from the expressions of the

chemical potential of carbon dissolved in nickel and carbon in the segregated layer. Finally, the time-dependence of the carbon concentration in the segregated layer is simply obtained using the following equation (Eq.8):

$$\frac{\partial C_s}{\partial t} = J \quad (\text{Eq.8})$$

The differential equations above were solved using a finite difference method implemented in a bespoke Matlab program. The ode15s solver[42] was used.

Fitting was performed. On one hand, the calculated C_I concentration (concentration in the bulk just below the segregated layer) was compared to the dissolved carbon content C_{dis} measured by XPS. On the other hand, the calculated C_s concentration (carbon concentration in the segregated layer) was compared to the XPS experimental values of $C_{Gr} + C_B$.

It should be mentioned here that only the carbon diffusion/segregation is addressed by the model. In contrast, nitrogen is not taken into account. Indeed XPS measurements show that the total apparent concentration of nitrogen is only of a few at.% at maximum. This includes the actual surface content (in the graphene layers) as well as possible nitrogen dissolved in the nickel bulk (subsurface). This means that both of these contents (surface and bulk) are below a few at%, even for long annealing times, which is very small. As a consequence, no particular effect of nitrogen on the diffusion/segregation behaviour of carbon is expected. In other words, the assumption of "infinite dilution" is fulfilled here as only about a few percents of the carbon atoms have a nitrogen atom located in a first neighbour interstitial site.

	Symbol	Value	Comment
Nickel thickness		150 nm	
Annealing temperature	T	500, 300 and 200 °C	
Number of nickel atoms per unit volume in nickel	C_{Ni}	$9.1 \cdot 10^{28} \text{ m}^{-3}$	
Maximum carbon concentration in the segregated layer	C_{Max}	$3.82 \cdot 10^{19} \text{ m}^{-2}$	See text
Fixed carbon concentration on the underside of nickel	C_i	7.0%at. at 500 °C 6.2% at. at 300 °C 4.5% at. at 200 °C	Adjusted
Carbon diffusion coefficient in well crystalized nickel	D	$2.48 \cdot 10^{-4} \exp\left(-\frac{168 \text{ kJ.mol}^{-1}}{RT(K)}\right) \text{ m}^2 \text{ s}^{-1}$	Lander[43]
Accelerated carbon diffusion coefficient	D	$1.1 \cdot 10^{-18} \text{ m}^2 \text{ s}^{-1}$ at 200 °C $3.0 \cdot 10^{-18} \text{ m}^2 \text{ s}^{-1}$ at 300 °C	Adjusted
Surface segregation free energy of carbon in nickel	ΔG	-18.8 kJ mol ⁻¹ at 500 °C -13.6 kJ mol ⁻¹ at 300 °C -9.8 kJ mol ⁻¹ at 200 °C	Adjusted

Table 3: Model inputs.

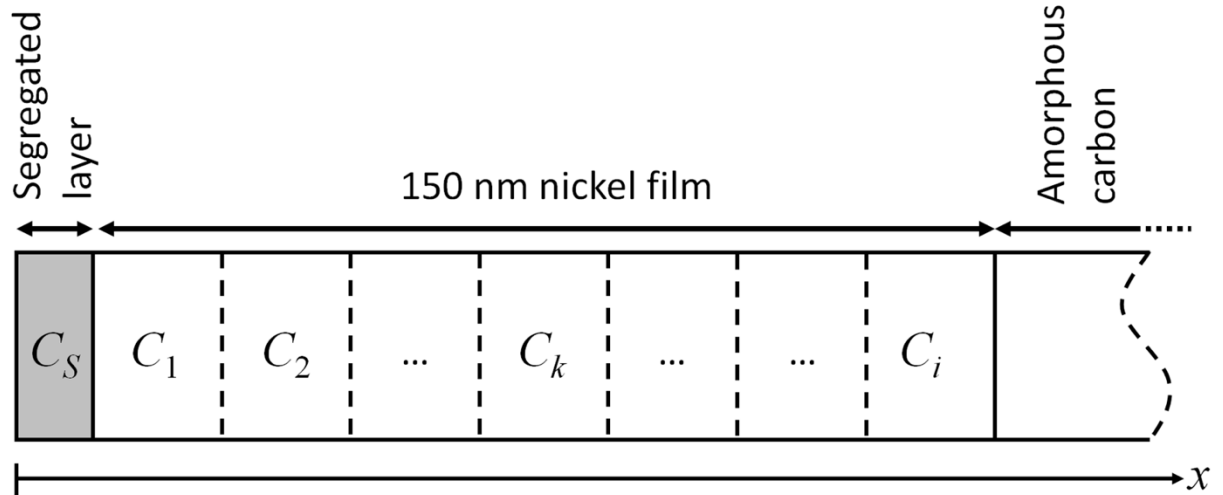


Figure 8: Principle of the diffusion/segregation model used to fit the experimental kinetics measured using XPS. C_i is considered to be constant over time at a given temperature (Dirichlet boundary condition). Meshing: one hundred slices in the 150 nm nickel film.

3.3.2. Model results

In the first step, bulk diffusion of carbon in nickel was assumed. Lander's temperature dependent diffusion coefficient was considered (see **Table 3**). The time dependences calculated for segregated carbon and for dissolved carbon at 200, 300 and 500 °C are shown in **Figure 9a** and **9b**, respectively, together with the corresponding experimental measurements. It should be recalled that the ramping rate used to reach the annealing temperature is 1K/s. The time at which the annealing temperature is reached is indicated by the arrows in **Figure 9**.

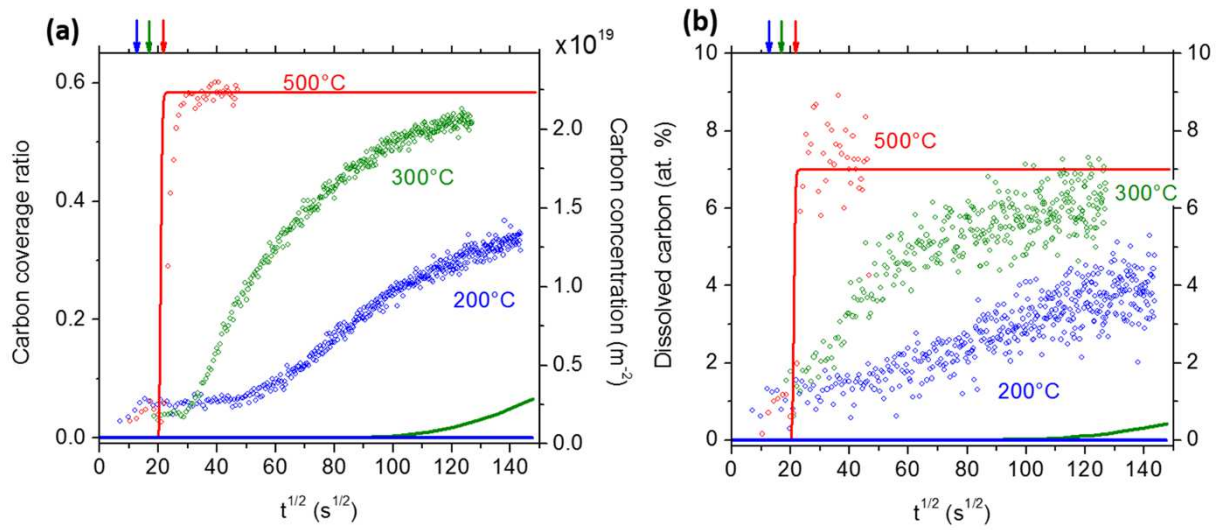


Figure 9: (a) Surface segregation kinetics of carbon during annealing at 200, 300 and 500 °C. The circles represent the experimental carbon surface concentrations ($C_{Gr} + C_B$) measured using XPS. The lines are calculated from the model using the bulk diffusion coefficient of carbon in nickel. Note that at 200 and 300 °C, the model predicts practically no carbon segregation (see blue and green lines close to zero concentration); (b) Time dependence of dissolved carbon concentration just below the segregated layer during annealing at 200, 300 and 500 °C. The circles are the experimental measurements (C_{dis}) using XPS. The lines are calculated from the model using the bulk diffusion coefficient of carbon in nickel. Note that at 200 and 300 °C, the model predicts practically no dissolved carbon (see blue and green lines close to zero concentration). In both figures, the arrows at the top indicate the time at which the annealing temperature is reached. Note that the temperature ramp (1 K/s) used to reach the annealing temperature was taken into account in the model.

The temperature dependence of the diffusion coefficient was taken into account in the model. The C_i and ΔG terms were adjusted to 7% at. and $-18.8 \text{ kJ mol}^{-1}$ respectively so as to obtain the correct dissolved and segregated carbon concentration at equilibrium at 500 °C. The model is in good agreement with the measurements of the specimen annealed at 500°C: a sudden rise in the concentration of dissolved and segregated carbon is observed at $t^{1/2} \approx 20 \text{ s}^{1/2}$, i.e. $t \approx 400 \text{ s}$, which corresponds to the very end of the temperature ramp ($T \approx 450 \text{ °C}$). The good agreement between the model and the measurements suggest that the

assumption of bulk diffusion of carbon is correct for the specimen annealed at 500 °C. However, this is not the case at all at the two other temperatures. The model shows almost no carbon segregated, or dissolved, even after 20,000 s at 200 °C or 300°C (**Figures 9**). This is in strong disagreement with the experimental data showing a significant amount of segregated and dissolved carbon at those temperatures. We can conclude that the effective diffusion coefficient of carbon in the nickel film at 200 °C and 300 °C is certainly far larger than the bulk diffusion coefficient used in the model. The diffusion behavior observed here is related to the nanostructure of the nickel deposit and the density of defects contained in it (vacancies, dislocations, grain boundaries). In the specimen annealed at 500 °C, the nickel deposit is likely to recover (or even recrystallize) very fast[44,45] so that carbon diffusion proceeds mainly in a recovered microstructure with a low defect density. However, at 200 °C and 300 °C, recovery apparently does not take place, or at least is much slower than at 500 °C. Consequently, the nickel continues to display a high defect density for longer, which strongly accelerates carbon diffusion[45,46].

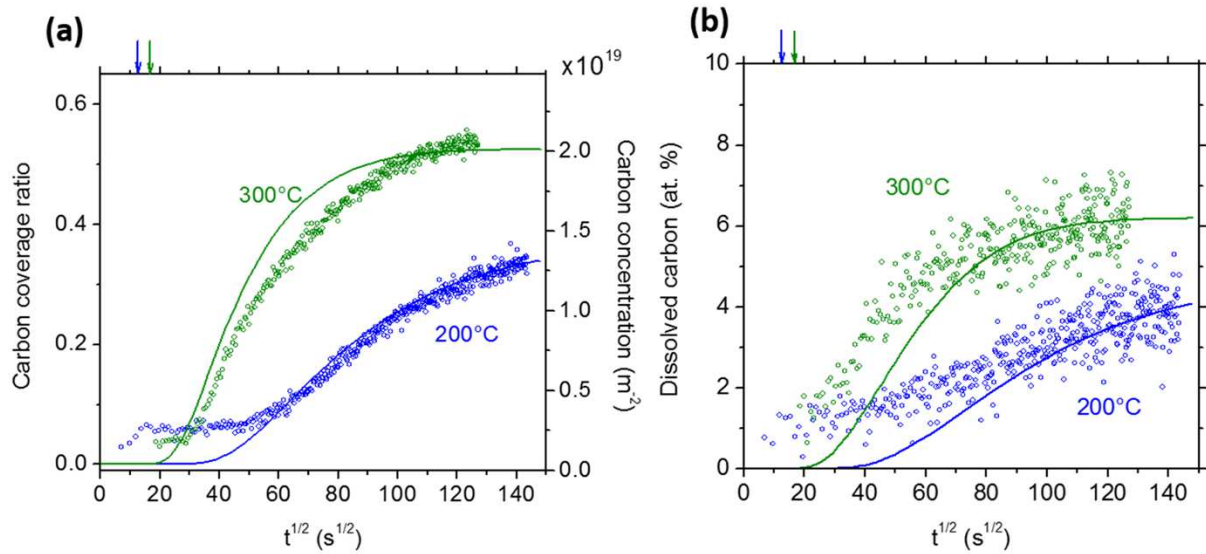


Figure 10: (a) Surface segregation kinetics of carbon during annealing at 200 and 300 °C. The circles represent the experimental carbon surface concentrations ($C_{Gr} + C_B$) measured using XPS. The lines are calculated from the model using an accelerated diffusion coefficient of carbon in nickel; (b) Time dependence of dissolved carbon concentration just below the segregated layer during annealing at 200 and 300 °C. The circles are the experimental measurements (C_{dis}) using XPS. The lines were calculated from the model using an accelerated diffusion coefficient of carbon in nickel. In both figures, the arrows at the top indicate the time at which the annealing temperature is reached. Note that this time, the temperature ramp (1K/s) used to reach the annealing temperature was not taken into account in the model.

In the second step, accelerated carbon diffusion was included in the model at 200 °C and 300 °C. Three terms had to be readjusted at each temperature to fit the time dependence of segregated ($C_{Gr} + C_B$) and dissolved (C_{dis}) carbon: accelerated diffusion coefficient,

segregation free energy, and the C_i term. The adjusted values are listed in **Table 3** and the plots are shown in **Figure 10**. The diffusion coefficient obtained by fitting at 200 and 300 °C is by one or several orders of magnitude higher than the Lander diffusion coefficient (bulk diffusion). The accelerating factor (ratio of the actual diffusion coefficient to the bulk diffusion coefficient) is 25 at 300 °C and is as high as 16,000 at 200 °C. This shows that the acceleration of diffusion due to the crystal defects in the nickel deposit is more efficient at low temperature, which is consistent with a higher defect density in the nickel deposit.

The following conclusions were inferred from modeling:

- In the specimen annealed at 500 °C, the transport of carbon across the nickel deposit is mainly governed by bulk diffusion. This can be explained by a very fast recovery of the nickel microstructure so that carbon diffusion takes place in a fully recovered microstructure.
- In contrast, the transport of carbon at 200 and 300°C is faster than bulk diffusion by one or several orders of magnitude. This is consistent with a very slow recovery of the nickel deposit. Consequently, the defect density remains very high, which allows accelerated diffusion of carbon.

4. Conclusion

Nitrogen-doped graphene growth was obtained by thermal heating using CN_x feedstock elaborated by pulsed laser deposition (PLD), covered by a thin layer of nickel catalyst. Our work demonstrates the elaboration of dominant pyrrolic nitrogen doped graphene with doping level close to 4 at.%. The aim of this work was focused on the understanding of the kinetics and mechanisms of carbon diffusion and segregation investigated by in situ XPS probing during the thermal heating process. XPS data were used to implement a model of diffusion/segregation of carbon through the nickel catalyst film. This study shows that in the same way than CVD method, growth of graphene domains from Ni atop carbon source at low temperature ($T < 500^\circ\text{C}$) is driven by the presence and content of subsurface carbon changing the interaction between graphene and catalyst, resulting in growth of domains of epitaxial monolayer to bilayer and rotated graphene as the amount of subsurface carbon increases. For $T > 500^\circ\text{C}$, our study points out the decomposition of metastable Ni_3C which can act as another catalyst phase in graphene growth.

Time resolved XPS measurement allowed to show also the primary role played by the microstructure and density of defects of the catalyst in the case of synthesis from a solid

carbon source. At low temperatures, the high defect density due to slow Ni microstructure recovery gives rise to accelerated transport of carbon, whereas at $T=500^{\circ}\text{C}$ the transport of carbon is mainly governed by bulk diffusion due to a fully recovered Ni microstructure. This aspect is of main importance as the amount of subsurface carbon, which influences the mechanism of graphene growth, is provided by the diffusion across the Ni layer catalyst. The diffusion/segregation model developed in this study can thus be used as a support to improve the graphene quality by a control of the amount of subsurface carbon, which is governed by the carbon diffusion across the nickel layer.

Acknowledgements

This work was conducted with the financial support of the Future Program Lyon Saint-Etienne (PALSE) in the framework of the LABEX MANUTECH-SISE (ANR-10-LABX-0075) from the University of Lyon (ANR-11-IDEX-0007), under the *Investissements d'Avenir* program managed by the French National Research Agency (French acronym ANR).

References

- [1] R.S. Weatherup, C. Baetz, B. Dlubak, B.C. Bayer, P.R. Kidambi, R. Blume, R. Schloegl, S. Hofmann, Introducing Carbon Diffusion Barriers for Uniform, High-Quality Graphene Growth from Solid Sources, *Nano Lett.* 13 (2013) 4624–4631.
- [2] W. Xiong, Y.S. Zhou, L.J. Jiang, A. Sarkar, M. Mahjouri-Samani, Z.Q. Xie, Y. Gao, N.J. Ianno, L. Jiang, Y.F. Lu, Single-Step Formation of Graphene on Dielectric Surfaces, *Advanced Materials.* 25 (2013) 630–634.
- [3] W. Xiong, Y.S. Zhou, W.J. Hou, T. Guillemet, J.F. Silvain, Y. Gao, M. Lahaye, E. Lebraud, S. Xu, X.W. Wang, D.A. Cullen, K.L. More, L. Jiang, Y.F. Lu, Solid-state graphene formation via a nickel carbide intermediate phase, *RSC Adv.* 5 (2015) 99037–99043.
- [4] D.T. Oldfield, C.P. Huynh, S.C. Hawkins, J.G. Partridge, D.G. McCulloch, Synthesis of multi-layer graphene films on silica using physical vapour deposition, *Carbon.* 123 (2017) 683–687.
- [5] Y. Bleu, F. Bourquard, T. Tite, A.-S. Loir, C. Maddi, C. Donnet, F. Garrelie, Review of Graphene Growth From a Solid Carbon Source by Pulsed Laser Deposition (PLD), *Front Chem.* 6 (2018).
- [6] A.M. Abd Elhamid, A.M. Aboulfotouh, M.A. Hafez, I.M. Azzouz, Room temperature graphene growth on complex metal matrix by PLD, *Diamond and Related Materials.* 80 (2017) 162–167.
- [7] N. Benchikh, F. Garrelie, C. Donnet, B. Bouchet-Fabre, K. Wolski, F. Rogemond, A.S. Loir, J.L. Subtil, Nickel-incorporated amorphous carbon film deposited by femtosecond pulsed laser ablation, *Thin Solid Films.* 482 (2005) 287–292.
- [8] N. Benchikh, F. Garrelie, C. Donnet, K. Wolski, R.Y. Fillit, F. Rogemond, J.L. Subtil, J.N. Rouzaud, J.Y. Laval, Nanostructured coatings of metal containing diamond-like carbon films deposited by femtosecond pulsed laser ablation, *Surface and Coatings Technology.* 200 (2006) 6272–6278.
- [9] F. Garrelie, N. Benchikh, C. Donnet, R.Y. Fillit, J.N. Rouzaud, J.Y. Laval, A. Pailleret, One-step deposition of diamond-like carbon films containing self-assembled metallic nanoparticles, by femtosecond pulsed laser ablation, *Appl. Phys. A.* 90 (2008) 211–217.
- [10] A. Sikora, A. Berkesse, O. Bourgeois, J.-L. Garden, C. Guerret-Piécourt, A.-S. Loir, F. Garrelie, C. Donnet, Electrical properties of boron-doped diamond-like carbon thin films deposited by femtosecond pulsed laser ablation, *Appl. Phys. A.* 94 (2009) 105–109.
- [11] A. Sikora, O. Bourgeois, J.C. Sanchez-Lopez, J.-N. Rouzaud, T.C. Rojas, A.-S. Loir, J.-L. Garden, F. Garrelie, C. Donnet, Effect of boron incorporation on the structure and electrical properties of diamond-like carbon films deposited by femtosecond and nanosecond pulsed laser ablation, *Thin Solid Films.* 518 (2009) 1470–1474.
- [12] C. Maddi, C. Donnet, A.-S. Loir, T. Tite, V. Barnier, T.C. Rojas, J.C. Sanchez-Lopez, K. Wolski, F. Garrelie, High N-content a-C:N films elaborated by femtosecond PLD with plasma assistance, *Applied Surface Science.* 332 (2015) 346–353.
- [13] S.R. Sarath Kumar, P.K. Nayak, M.N. Hedhili, M.A. Khan, H.N. Alshareef, In situ growth of p and n-type graphene thin films and diodes by pulsed laser deposition, *Appl. Phys. Lett.* 103 (2013) 192109.
- [14] P. Ren, E. Pu, D. Liu, Y. Wang, B. Xiang, X. Ren, Fabrication of nitrogen-doped graphenes by pulsed laser deposition and improved chemical enhancement for Raman spectroscopy, *Materials Letters.* 204 (2017) 65–68.
- [15] C. Maddi, F. Bourquard, V. Barnier, J. Avila, M.-C. Asensio, T. Tite, C. Donnet, F. Garrelie, Nano-Architecture of nitrogen-doped graphene films synthesized from a solid CN source, *Scientific Reports.* 8 (2018) 3247.

- [16] R.S. Weatherup, B.C. Bayer, R. Blume, C. Ducati, C. Baehtz, R. Schlögl, S. Hofmann, In Situ Characterization of Alloy Catalysts for Low-Temperature Graphene Growth, *Nano Lett.* 11 (2011) 4154–4160.
- [17] R.S. Weatherup, H. Amara, R. Blume, B. Dlubak, B.C. Bayer, M. Diarra, M. Bahri, A. Cabrero-Vilatela, S. Caneva, P.R. Kidambi, M.-B. Martin, C. Deranlot, P. Seneor, R. Schloegl, F. Ducastelle, C. Bichara, S. Hofmann, Interdependency of Subsurface Carbon Distribution and Graphene–Catalyst Interaction, *J. Am. Chem. Soc.* 136 (2014) 13698–13708.
- [18] R.S. Weatherup, A.J. Shahani, Z.-J. Wang, K. Mingard, A.J. Pollard, M.-G. Willinger, R. Schloegl, P.W. Voorhees, S. Hofmann, In Situ Graphene Growth Dynamics on Polycrystalline Catalyst Foils, *Nano Lett.* 16 (2016) 6196–6206.
- [19] A.C. Ferrari, Raman spectroscopy of graphene and graphite: Disorder, electron–phonon coupling, doping and nonadiabatic effects, *Solid State Communications*. 143 (2007) 47–57.
- [20] L.M. Malard, M.A. Pimenta, G. Dresselhaus, M.S. Dresselhaus, Raman spectroscopy in graphene, *Physics Reports*. 473 (2009) 51–87.
- [21] L.G. Cançado, K. Takai, T. Enoki, M. Endo, Y.A. Kim, H. Mizusaki, A. Jorio, L.N. Coelho, R. Magalhães-Paniago, M.A. Pimenta, General equation for the determination of the crystallite size L_a of nanographite by Raman spectroscopy, *Appl. Phys. Lett.* 88 (2006) 163106.
- [22] L.L. Patera, C. Africh, R.S. Weatherup, R. Blume, S. Bhardwaj, C. Castellarin-Cudia, A. Knop-Gericke, R. Schloegl, G. Comelli, S. Hofmann, C. Cepek, In Situ Observations of the Atomistic Mechanisms of Ni Catalyzed Low Temperature Graphene Growth, *ACS Nano*. 7 (2013) 7901–7912.
- [23] Gy.J. Kovács, I. Bertóti, G. Radnóczy, X-ray photoelectron spectroscopic study of magnetron sputtered carbon–nickel composite films, *Thin Solid Films*. 516 (2008) 7942–7946.
- [24] M. Jiao, K. Li, W. Guan, Y. Wang, Z. Wu, A. Page, K. Morokuma, Crystalline Ni_3C as both carbon source and catalyst for graphene nucleation: a QM/MD study, *Scientific Reports*. 5 (2015) 12091.
- [25] R. Yadav, C.K. Dixit, Synthesis, characterization and prospective applications of nitrogen-doped graphene: A short review, *Journal of Science: Advanced Materials and Devices*. 2 (2017) 141–149.
- [26] J. Soo Kang, M.-A. Park, J.-Y. Kim, S. Ha Park, D. Young Chung, S.-H. Yu, J. Kim, J. Park, J.-W. Choi, K. Jae Lee, J. Jeong, M. Jae Ko, K.-S. Ahn, Y.-E. Sung, Reactively sputtered nickel nitride as electrocatalytic counter electrode for dye- and quantum dot-sensitized solar cells, *Scientific Reports*. 5 (2015) 10450.
- [27] L. Wang, Z. Sofer, J. Luxa, M. Pumera, Nitrogen doped graphene: influence of precursors and conditions of the synthesis, *J. Mater. Chem. C*. 2 (2014) 2887–2893.
- [28] H.L. Poh, P. Šimek, Z. Sofer, I. Tomandl, M. Pumera, Boron and nitrogen doping of graphene via thermal exfoliation of graphite oxide in a BF_3 or NH_3 atmosphere: contrasting properties, *J. Mater. Chem. A*. 1 (2013) 13146–13153.
- [29] Y. Cao, W. Si, Y. Zhang, Q. Hao, W. Lei, X. Xia, J. Li, F. Wang, Nitrogen-doped graphene: Effect of graphitic-N on the electrochemical sensing properties towards acetaminophen, *FlatChem*. 9 (2018) 1–7.
- [30] P. Tyagi, Z.R. Robinson, A. Munson, C.W. Magnuson, S. Chen, J.D. McNeilan, R.L. Moore, R.D. Piner, R.S. Ruoff, C.A. Ventrice, Characterization of graphene films grown on CuNi foil substrates, *Surface Science*. 634 (2015) 16–24.
- [31] B.C. Bayer, D.A. Bosworth, F.B. Michaelis, R. Blume, G. Habler, R. Abart, R.S. Weatherup, P.R. Kidambi, J.J. Baumberg, A. Knop-Gericke, R. Schloegl, C. Baehtz,

- Z.H. Barber, J.C. Meyer, S. Hofmann, In Situ Observations of Phase Transitions in Metastable Nickel (Carbide)/Carbon Nanocomposites, *J. Phys. Chem. C.* 120 (2016) 22571–22584.
- [32] M. Batzill, The surface science of graphene: Metal interfaces, CVD synthesis, nanoribbons, chemical modifications, and defects, *Surface Science Reports.* 67 (2012) 83–115.
- [33] K. Natesan, T.F. Kassner, Thermodynamics of carbon in nickel, iron-nickel and iron-chromium-nickel alloys, *MT.* 4 (1973) 2557–2566. doi:10.1007/BF02644258.
- [34] M. Singleton, P. Nash, The C-Ni (Carbon-Nickel) system, *Bulletin of Alloy Phase Diagrams.* 10 (1989) 121–126.
- [35] K.T. Jacob, S. Seetharaman, Thermodynamic stability of metallurgical coke relative to graphite, *MMTB.* 25 (1994) 149–151.
- [36] J. du Plessis, G.N. van Wyk, A model for surface segregation in multicomponent alloys—part III: The kinetics of surface segregation in a binary alloy, *Journal of Physics and Chemistry of Solids.* 50 (1989) 237–245.
- [37] F. Fournier Dit Chabert, F. Tancrét, F. Christien, R. Le Gall, J.-F. Castagné, Finite element simulation of interfacial segregation in dilute alloys, *J Mater Sci.* 42 (2007) 9765–9774.
- [38] J.Y. Wang, J. du Plessis, J.J. Terblans, G.N. van Wyk, Kinetics near the discontinuous surface transition in the Cu(Ag)(111) binary segregating system, *Surface Science.* 423 (1999) 12–18.
- [39] E.C. Viljoen, W.A. Jordaan, J. du Plessis, On the determination of ternary segregation parameters, *Vacuum.* 61 (2001) 141–144.
- [40] F. Tancrét, F. Fournier Dit Chabert, F. Christien, R. Le Gall, Finite element simulation of complex interfacial segregation phenomena in dilute alloys, *J Mater Sci.* 44 (2009) 4604–4612.
- [41] F. Christien, R. Le Gall, G. Saindrenan, Application of percolation theory to surface segregation during recovery, *Acta Materialia.* 51 (2003) 521–534.
- [42] L. Shampine, M. Reichelt, The MATLAB ODE Suite, *SIAM J. Sci. Comput.* 18 (1997) 1–22.
- [43] J.J. Lander, H.E. Kern, A.L. Beach, Solubility and Diffusion Coefficient of Carbon in Nickel: Reaction Rates of Nickel-Carbon Alloys with Barium Oxide, *Journal of Applied Physics.* 23 (1952) 1305–1309.
- [44] J.E. Darnbrough, P.E.J. Flewitt, Growth of abnormal planar faceted grains in nanocrystalline nickel containing impurity sulphur, *Acta Materialia.* 79 (2014) 421–433.
- [45] F.J. Humphreys, M. Hatherly, *Recrystallization and Related Annealing Phenomena*, Elsevier, 2012.
- [46] R. Le Gall, G. Saindrenan, Effects of Metastable Diffusion Short-Circuits on Surface Segregation, *Interface Science.* 11 (2003) 59–66.

Intensity (au)

